ACS Energy LETTERS

http://pubs.acs.org/journal/aelccp

LETTER

Transport and Thermodynamic Properties of KFSI in TEP by Operando Raman Gradient Analysis

Junyi Zhao, Ben Jagger,† Lorenz F. Olbrich,† Johannes Ihli, Shobhan Dhir, Maxim Zyskin, Xinyao Ma, and Mauro Pasta*

Cite This: ACS Energy Lett. 2024, 9, 1537−1544

Read Online

ACCESS | Metrics & More | Article Recommendations | Supporting Information

ABSTRACT: Understanding and characterizing the transport and thermodynamic properties of electrolytes are critical for optimizing battery performance. In this study, we employ operando Raman gradient analysis (ORGA) to characterize the concentration-dependent diffusion coefficient, transference number, ionic conductivity, and thermodynamic factor of potassium bis(fluorosulfonyl)imide (KFSI) in triethyl phosphate (TEP), an ideal model system and one of the most promising K-ion battery electrolytes. ORGA demonstrates results consistent with conventional state-of-the-art methods while proving to be significantly more electrolyte- and time-efficient. Additionally, we probe, for the first time, the concentration-dependent transport and thermodynamic properties of KFSI-TEP, providing key parameters for K-ion battery modeling.

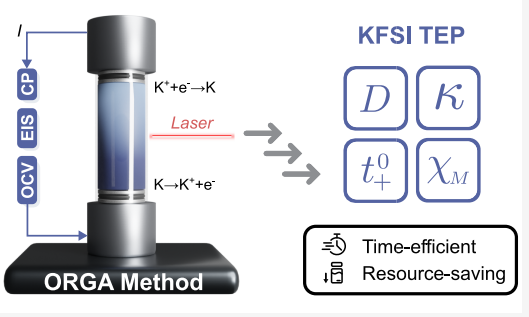

1. INTRODUCTION

The global battery demand is projected to rise significantly in the near future, driven primarily by electrification of transportation.[1] Uncertain supply chains and increasing procurement costs of critical elements essential to lithium-ion battery (LIB) production, including lithium, nickel, cobalt, and copper,[2,3] are fueling the development of a new generation of battery chemistries utilizing elements with greater supply security, such as sodium and potassium.[4−6] Potassium-ion batteries (KIBs) are particularly promising owing to their competitive cost and the ability to utilize graphite anodes and critical-mineral-free cathodes.[4] Despite their potential, KIBs are still in the early stages of development, requiring electrolyte optimization, among other factors, for successful commercialization. Previous research has made significant progress in addressing electrolyte compatibility with electrode materials and aluminum current collectors,[5,7] but electrolyte transport properties are rarely reported or considered.

Electrolyte ionic transport processes are typically much slower than electron transfer, thereby constraining battery performance like charge−discharge rate capability[8−11] and low-temperature operation.[10,11] Additionally, ionic transport influences battery degradation due to the formation of concentration gradients, which promote interfacial side reactions and negatively affect cycle life.[8,12] Furthermore, nonuniform concentration may accelerate the formation and growth of dendrites,[13] causing short circuits and their associated safety concerns.[14,15] Therefore, understanding and characterizing electrolyte ionic transport is critical to optimize battery performance and probe battery degradation.[12,15,16]

A suite of electrolyte transport and thermodynamic properties has been defined to elucidate ionic transport, encompassing the diffusion coefficient, D, cation transference number, t_+^0, ionic conductivity, κ, thermodynamic factor, χ_M, and partial molar volumes of salt and solvent, $\bar{V}_s$ and $\bar{V}_0$, respectively.[17] A diverse array of experimental methods are utilized to measure these properties including electroanalytical techniques,[8,9,18−31] thermodynamic methodologies,[20,32,33] and computational simulations.[34] However, these conventional methods suffer from various drawbacks. First, Mistry and Srinivasan have commented that self-diffusion measurement methods like pulse field gradient nuclear magnetic resonance (pfg-NMR) are not directly related to ionic transport in polarized electrolytes and should not be used to calculate diffusion coefficients.[35] In addition, methods such as the Bruce−Vincent approach rely on unachievable theoretical

Received: March 5, 2024
Accepted: March 8, 2024

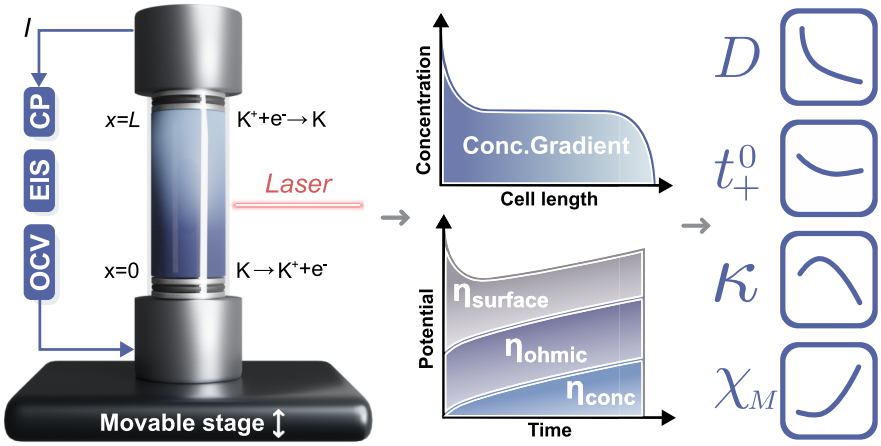

Figure 1. Schematic of operando Raman gradient analysis (ORGA) to measure electrolyte properties. The ORGA cell, a custom-built electrochemical cell, consists of two stainless steel pistons and an optical quartz tube. O-rings and external sealant are used to prevent electrolyte leakage and isolate the system from the surrounding atmosphere. An internal electrolyte concentration gradient is established in the symmetrical system during electrode polarization, and 1D Raman line scans are used to measure the development of a concentration gradient across the cell. The polarization process is monitored using chronopotentiometry (CP), electrochemical impedance spectroscopy (EIS), and open-circuit voltage (OCV) to separate the overpotential contributions. The concentration and potential functions are then incorporated into the CST model to determine key transport and thermodynamic properties. Further details, including a parametric description are provided in Note S2.

assumptions, such as electrolyte ideality.[26,27] Moreover, most of these techniques can only be used to measure a single electrolyte property per measurement series, so achieving a comprehensive characterization of key properties for electrolytes often entails a significant number of experimental apparatuses, onerous procedures, and practical challenges.

There are also several techniques with the capability to directly visualize concentration distributions in the electrolyte, utilizing NMR,[16,36−42] X-ray,[11,15,43−46] Raman,[47−50] UV,[12] visible light,[13,51] and neutron spectroscopy,[52] for example. When combined with simultaneous measurements of the electrode potential over time, these techniques could enable the complete set of transport and thermodynamic properties to be obtained through the ionic flux laws and the modified Ohm's law from concentrated solution theory (CST), all within a single measurement series and experimental setup. Our group has demonstrated the feasibility of this approach previously using operando Raman microspectroscopy combined with electrochemical impedance spectroscopy EIS,[48] which we have further developed into "operando Raman gradient analysis (ORGA)".

Here, we elaborate on ORGA, offering additional insights into experimental and data processing optimization and theory to enhance its capabilities. These advances are demonstrated by determining, for the first time, the transport and thermodynamic properties (κ, D, t_+^0 and χ_M) of potassium bis(fluorosulfonyl)imide (KFSI) in triethyl phosphate (TEP). KFSI-TEP was selected as it is a promising electrolyte in the K-ion research community,[53−55] but a comprehensive study of ionic transport in this system has not been reported. The characterization of KFSI-TEP requires the implementation of potassium metal electrodes, the high reactivity of which makes electrolyte characterization challenging,[56] demonstrating the versatility of ORGA. We further independently measure the transport properties using four conventional state-of-the-art methods, including restricted diffusion, the densitometric Hittorf method, concentration cells, and EIS, demonstrating that ORGA exhibits results consistent with those obtained through conventional methods, while providing a more time- and electrolyte-efficient avenue to measure these properties.

We subsequently utilize ORGA to investigate the concentration dependence of κ, D, t_+^0, and χ_M of KFSI-TEP over a concentration range of 1−3 m, enabling deeper insight into the transport behavior and providing critical parameters for battery modeling. Overall, ORGA facilitates a more rapid and cost-effective electrolyte characterization with the potential to accelerate "beyond lithium-ion battery" research.

2. OPERANDO RAMAN GRADIENT ANALYSIS TECHNIQUE (ORGA)

A schematic representation of the ORGA is shown in Figure 1. We perform chronopotentiometry (CP), EIS, and open-circuit voltage (OCV) measurements during galvanostatic polarization to establish a concentration gradient. CP captures the cell potential, encompassing the Ohmic drop, η_{Ohmic}, concentration overpotential, η_{conc}, and complex changes occurring on the electrode surface, $\eta_{surface}$. EIS aids in determining η_{Ohmic} and $\eta_{surface}$, allowing η_{conc} to be calculated. Short periods of the OCV also provide direct access to η_{conc}.

During the polarization, Raman line scans are performed at selected intervals, from the anodic to the cathodic electrode (Figure S1). Each Raman spectrum is converted into a salt concentration through a calibration curve, determined by collecting Raman spectra at various concentrations with a confocal Raman microspectrometer (Renishaw inVia Reflex, Figure S2). These spectra are plotted in Figure 2a along with the Raman-active vibrational modes for FSI^- and TEP. The $-CH_3$ rocking vibration of TEP is chosen as an internal reference for spectrum normalization (due to its high intensity and clear separation from FSI^- peaks) to eliminate laser pulse fluctuations and other potential influences on signals (Figure S3a). Figure 2a illustrates the trend of normalized signals in the range 600−1800 cm^{-1} with respect to electrolyte concentration. It is evident that the peak intensity in the 680−780 cm^{-1} range significantly increases with increasing electrolyte

https://doi.org/10.1021/acsenergylett.4c00661
ACS Energy Lett. 2024, 9, 1537−1544

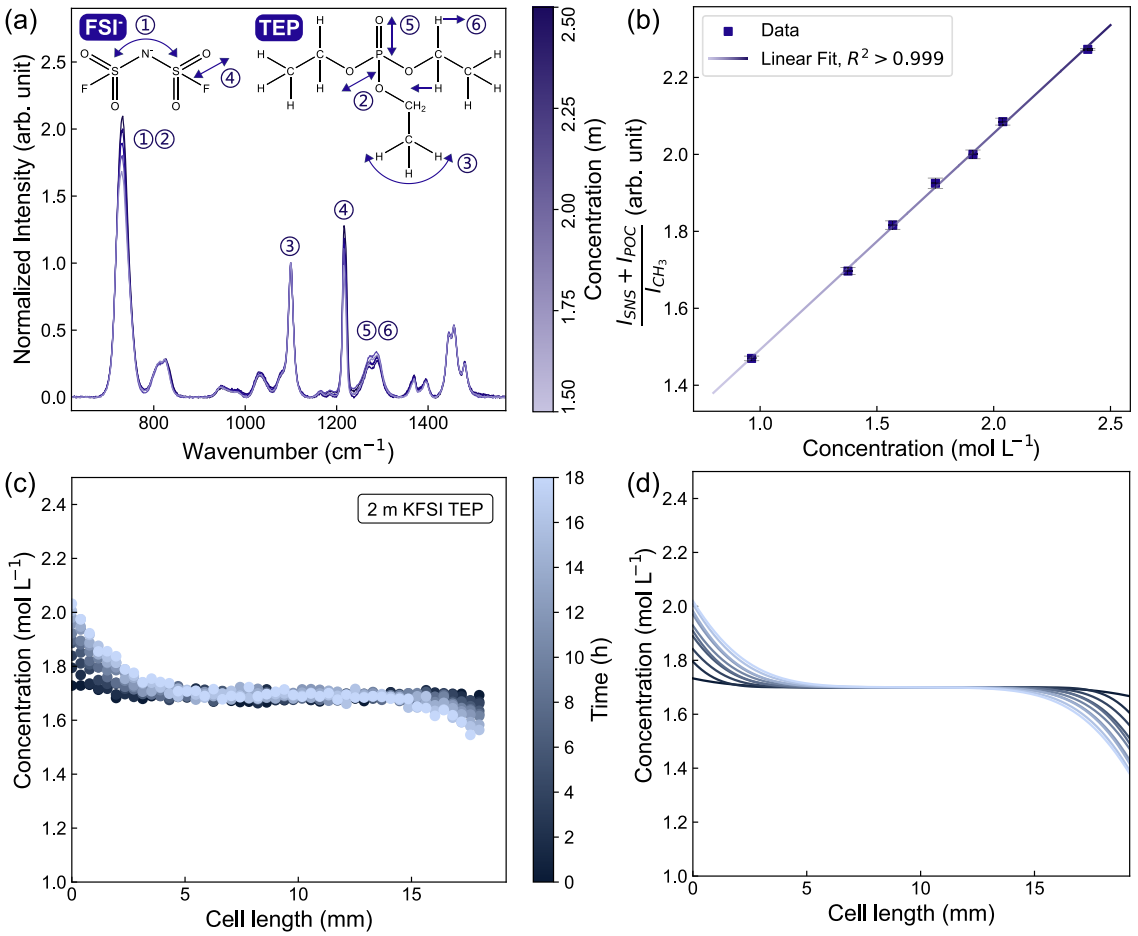

Figure 2. (a) Normalized Raman spectra of KFSI-TEP electrolyte from 600 to 1800 cm^{-1} with varying concentration. Molecular structure diagrams of the anion (FSI^-) and solvent (TEP) are shown in the inset. Raman band-molecular vibration mode assignments in KFSI-TEP are as follows: the 680−780 cm^{-1} band, increasing in intensity with concentration, originates mainly from the FSI^- S−N−S stretching vibration (1),[48] and also includes the TEP P−O−(C) stretching vibration (2); the band at ∼1100 cm^{-1} represents the $-CH_3$ rocking vibration in TEP (3);[55] the band from 1200 to 1230 cm^{-1} represents the S═O vibration from FSI^- (4);[54,55,58] the bands from 1250−1320 cm^{-1} may involve the P═O vibration from TEP (5) and the CH_2 twisting vibration (6).[54] (b) Calibration curve converting the normalized 680−780 cm^{-1} band intensity to salt concentration, used to determine the concentration gradient via operando Raman microspectroscopy. Error bars represent the standard deviation calculated from three repeat measurements. (c) The measured concentration gradient evolution of 2 *m* (1.752 M) KFSI-TEP during polarization for 18 h at 20 °C, with i = 100 μA cm^{-2} (Figure S5 presents the gradients in salt:solvent ratio). (d) The corresponding concentration gradient profile fit, based on a symmetric cell polarization model detailed in Note S2. The color denotes polarization time.

concentration. Despite the overlap of the P−O−(C) stretching vibration in TEP and the S−N−S bending vibration in FSI^- within this band,[48,57] spectral analysis reveals that the S−N−S stretching vibration signal, generated by the introduction of FSI^-, dominates the variation in this band. As a result, the difference in the P−O−(C) vibration minimally influences the maximum intensity of the peak. Double pseudo-Voigt fitting was performed on the 680−780 cm^{-1} band to obtain $\frac{I_{SNS}+I_{POC}}{I_{CH_3}}$ (Figure S3b), enabling the calibration curve to be established (Figure 2b). This calibration curve exhibits a linear correlation (R^2 > 0.999). Calibration using the S═O vibration was also explored (Figure S4), but the results displayed greater noise than in Figure 2b because fluorescence from quartz at this wavenumber affects the background correction.

Figure 2c tracks the temporal and spatial changes in concentration within the ORGA cell during galvanostatic polarization (i = 100 μA cm^{-2}, T = 20 ± 0.3 °C) for a 2 *m* KFSI-TEP electrolyte, demonstrating the formation of a concentration gradient and its progression into the cell over time. We additionally conducted a laser power−electrolyte degradation test and signal-to-noise ratio analysis for different laser powers (Figure S6), revealing that lower laser power resulted in a highly dispersed concentration signal (Figure S7). In this experiment, we therefore selected the maximum laser power (300 mW), as this gave the highest signal-to-noise ratio, with no evidence of electrolyte degradation.

Note S2 provides a detailed derivation of the symmetric cell polarization model based on the CST. Figure 2d displays the gradient after fitting the raw concentration data using this model. To improve fitting and subsequent data processing, signals close to the cathodic side of the cell were excluded because of evidence that nonuniform deposition affected the Raman signal, reducing the reliability of data gathered close to the cathodic electrode (Figure S8). This effectively helped reduce fitting errors (Table S1). The fit of the concentration functional form with this model closely aligns with the data, with the fitting quality parameter (χ^2) primarily falling within

https://doi.org/10.1021/acsenergylett.4c00661
ACS Energy Lett. 2024, 9, 1537−1544

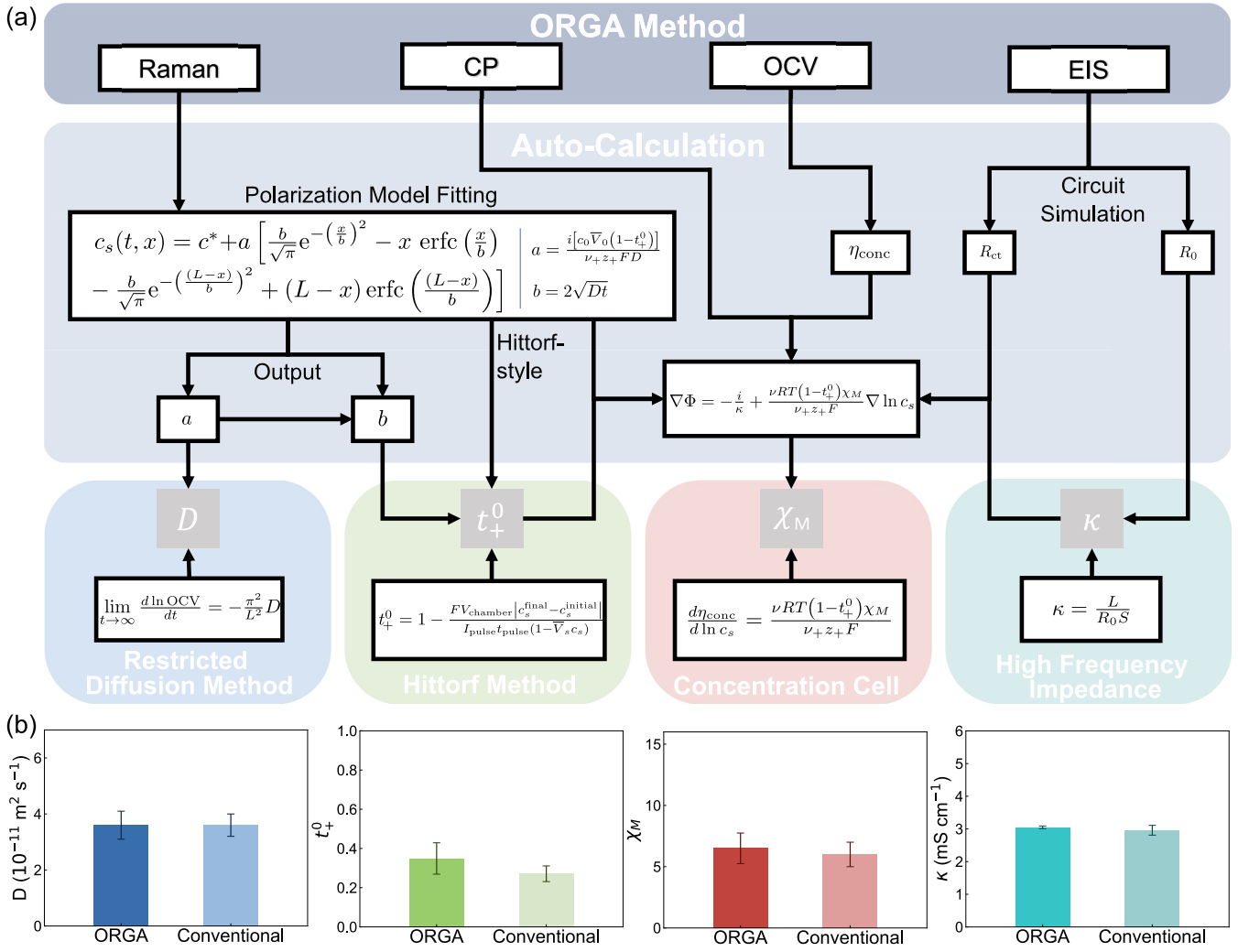

Figure 3. (a) Workflows illustrating the calculation steps needed to determine electrolyte transport properties via ORGA and selected conventional methods. R_{ct} stands for charge-transfer resistance and contributes to the surface overpotential. R_0 represents bulk resistance and is responsible for the Ohmic drop. The concentration overpotential can be either calculated by cell potential (CP data) minus $I(R_{ct} + R_0)$ or measured directly by OCV. The Φ shown in the bluish-gray section is the ideal cell potential in the equation, which means no surface overpotential is considered. The necessary partial molar volumes and solvent velocity factor $\left(1 - \frac{d\ln c_0}{d\ln c_s}\right)$ for computations were predominantly acquired through densitometry (Figure S9). Provided in Note S2 are further details including derivations. (b) Comparison of transport and thermodynamic properties obtained by ORGA and conventional methods.

Table 1. Comparion of Transport and Thermodynamic Properties of 2 *m* KFSI in TEP at 20°C Determined by ORGA and Conventional Methods

method	D (10^{-11} m^2 s^{-1})	t_+^0	χ_M	κ (mS cm^{-1})
ORGA	3.6 ± 0.5	0.35 ± 0.08	6.5 ± 1.2	3.05 ± 0.04
conventional	3.6 ± 0.4	0.27 ± 0.04	6.0 ± 1.0	2.96 ± 0.15

0−0.005 (Table S1). This initial part of the study presents a successful case of concentration gradient visualization and an improved fitting strategy.

3. COMPARISON WITH CONVENTIONAL METHODS

Our group's prior research introduced the computation of key transport and thermodynamic properties using concentration gradients and electrochemical data.[48] This process was refined, streamlining the computational procedures, as depicted in Figure 3a. The transport and thermodynamic properties of 2 *m* KFSI-TEP determined by using ORGA are shown in Figure 3b. Figure S10 presents data from three parallel experiments demonstrating excellent repeatability. Additionally, conventional state-of-the-art methods (the restricted diffusion method, densitometric Hittorf method, concentration cell, and high-frequency impedance method) were independently employed to measure these properties, as illustrated in Figure 3a. Figure 3b and Table 1 demonstrate the excellent consistency between the results gathered using ORGA and those measured by the leading conventional methods. ORGA gives properties with approximately the same level of uncertainty as the traditional methods, and all values are in agreement between the two approaches. Moreover, higher concentration electrolytes (e.g., 2 *m*) often exhibit more

https://doi.org/10.1021/acsenergylett.4c00661
ACS Energy Lett. 2024, 9, 1537−1544

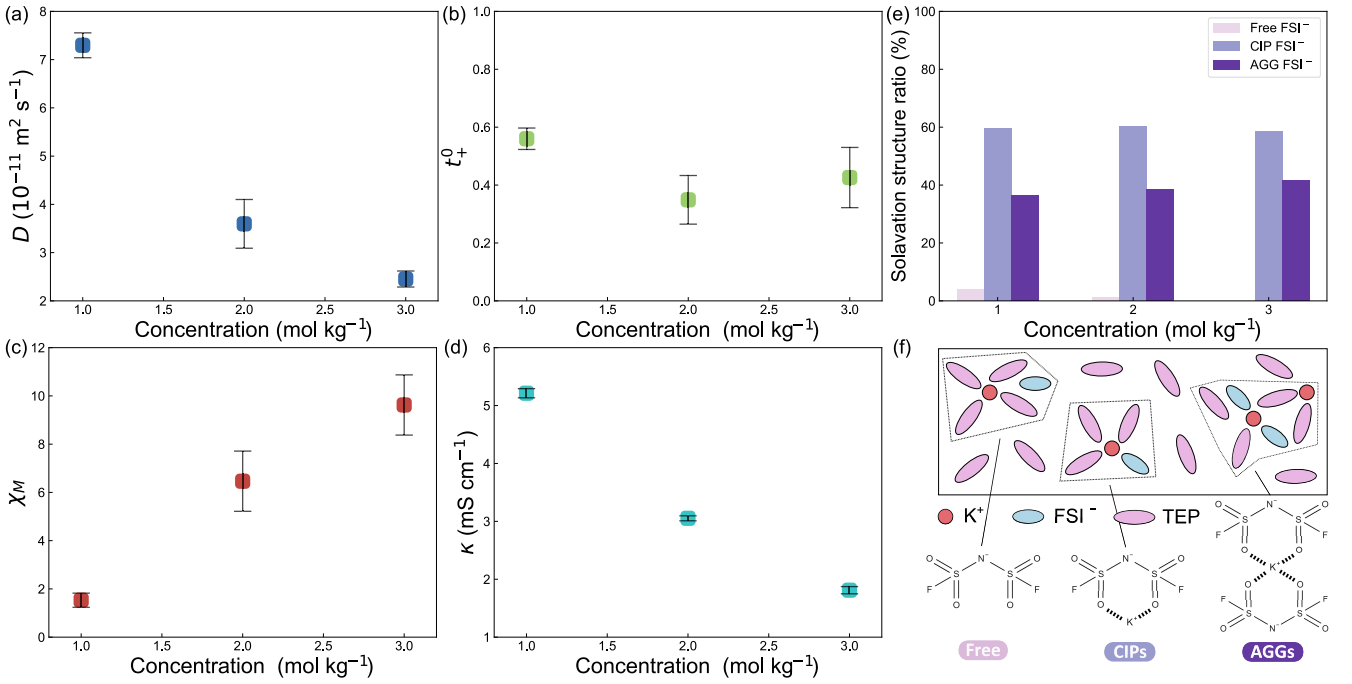

Figure 4. Concentration-dependent transport and thermodynamic properties KFSI in TEP measured using ORGA. Properties were determined at 1 *m* (0.963 M), 2 *m* (1.752 M) and 3 *m* (2.412 M) at 20 °C (unit conversion in Table S5). (a) Diffusion coefficient. (b) Cation transference number. (c) Thermodynamic factor. (d) Ionic conductivity. (e) Breakdown of FSI^- solvation structures as a function of concentration, derived from the S═O vibration using Raman spectroscopy. (f) Schematic representation of three FSI^- solvation structures. The AGGs structure represents two or more FSI^- in the inner solvation sheath of a single K^+.

pronounced nonideal behavior,[14] and the conventional techniques are currently the most accurate methods of transport property determination,[24,56] enhancing the broader significance of the consistency observed in this study.

In addition to providing the same information as conventional methods, ORGA has several advantages. The ORGA cell has a simple design and can simultaneously give all relevant transport and thermodynamic properties in a single experimental setup, whereas different cell designs and procedures are required to measure each property using conventional methods. Once a density curve and calibration line have been produced, ORGA can be used to fully characterize a single electrolyte concentration in a short amount of time. In contrast, a single restricted diffusion measurement can take upward of 3 days. ORGA also requires significantly less electrolyte than conventional methods. Figure S11 presents a comparison between the electrolyte volumes and measurement times required by both ORGA and the conventional methods, demonstrating that ORGA is significantly less resource- and time-intensive. Based on quantitative analysis in our case (Figure S11), for a full characterization experiment (single repeat), ORGA saves approximately 98% of the electrolyte and reduces electrochemical measurement time by 82% in total, although it should be noted that electrolyte and time savings will depend on the user and the system under investigation. Additionally, through analysis of the Raman spectra, ORGA offers direct insight into the bulk electrolyte solvation behavior. ORGA is therefore well suited for rapid and accurate electrolyte characterization.

4. CONCENTRATION DEPENDENCE OF PROPERTIES

We therefore further employed ORGA to investigate the concentration dependence of the transport and thermodynamic properties of KFSI-TEP within the concentration range of 1−3 *m*. This concentration range was selected based on the proven performance of 2 and 2.5 M KFSI-TEP in full-cell K-ion batteries.[53,54] Figure 4a−d shows the concentration dependence of the properties. First, the diffusion coefficient gradually decreases with increasing concentration (Figure 4a), aligning with the typical trend of concentration-dependent diffusion coefficients. This is attributed to the enhanced ion−ion and ion−solvent interactions (friction between ions and solvent) at higher concentrations, hindering the diffusion behavior. The declining trend in ionic conductivity (Figure 4d) is also attributed to the continuous strengthening of those interactions beyond 1 *m*, limiting the migration capability of the ions. Even with a higher concentration of ions in the system, there is no improvement in migration velocity. The observed increase in viscosity from 2 to 3 *m*, as depicted in Figure S12, supports these trends.

The cation transference number exhibits an initial decrease from 1 to 2 *m* and then remains constant within experimental uncertainty from 2 to 3 *m* (Figure 4b). This trend is consistent with previous reports from both Li- and K-ion electrolytes[20,32,56] and suggests that the ion−ion and ion−solvent interactions that occur at higher concentration bind K^+ more strongly than the FSI^-.

To further understand these concentration dependencies we examined the Raman FSI^- S═O vibrational signal to investigate anion solvation from 1 to 3 *m* (Figure S13). Consistent with the literature, we identify three peaks, which we separated with a triple pseudo-Voigt fitting, corresponding to free FSI^- at 1209 cm^{-1}, and to FSI^- in contact-ion pairs (CIPs) and aggregates (AGGs) at 1215 and 1220 cm^{-1}, respectively.[58] These solvation structures are depicted schematically in Figure 4f. The results (Figure 4e) show that

https://doi.org/10.1021/acsenergylett.4c00661
ACS Energy Lett. 2024, 9, 1537−1544

the majority of FSI^- exists in the form of CIPs at all concentrations considered. The amount of free FSI^- decreases with increasing concentration (4.03, 1.33, and 0.00% for 1, 2, and 3 *m* respectively). At the same time, the proportion of AGGs increases with concentration (36.37, 38.55, and 41.58% for 1, 2, and 3 *m*, respectively), consistent with the higher viscosity observed at 3 *m* and the decreasing D and κ with increasing concentration. We categorize ion migration into two main mechanisms: vehicular (the solvated shell) motion and ion hopping mechanism (ligand exchange). Based on the observed trends in solvation structures, we infer the following: in the 1−2 *m* range, the increase in negatively charged AGGs counteracts the K^+ vehicular motion, leading to a decrease in the cation transference number. Subsequently, in the 2−3 *m* range (more viscous), the bulky AGG structures become relatively immobile, and we speculate that the hopping mechanism of K^+ dominates, disrupting the decreasing trend of cation transference number, reaching a plateau. This aligns with discussions by Yu et al. regarding the impact of aggregates on ion migration.[59]

For the thermodynamic factor, we observe a rapid increase with increasing concentration (Figure 4c). Typically, the thermodynamic factor at low concentration is influenced by the dominance of long-range ion−ion association (the extent is dependent on the dielectric constant of the solvent), leading to a reduction in the thermodynamic factor. Subsequently, the increase in salt concentration results in the solvent becoming increasingly bound (where solvation effects predominate), with insufficient free solvent available to bind and stabilize the potassium ions, causing the thermodynamic factor to rise rapidly. The obtained thermodynamic factor is already greater than 1 at 1 *m*, indicating that at this point, the majority of TEP has already been bound. Liu et al. calculated that approximately 70% of the TEP is solvated in the range 1.5−2 M. Additionally, the solvation ratio (solvated TEP:K^+) decreases from 2.1:1 at 1.5 M to 1.1:1 at 2.5 M,[54] indicating a lack of sufficient free TEP to solvate potassium ions; hence, FSI^- is able to enter into the inner solvation sheath of the K^+, consistent with the prevalence of CIPs and AGGs evident in Figure 4e.

This section of the study delineates the trends within the 1−3 *m* concentration range, providing deeper insights into the transport behavior of KFSI-TEP. It also provides critical properties for battery modeling.[60] The results indicate that, within this concentration range, lower concentrations exhibit better transport performance (higher D, κ and t_+^0) with comparatively lower concentration overpotential (smaller χ_M). While the current literature affirms sufficient interface stability of 2 and 2.5 M KFSI-TEP,[53,54] transport properties are vital for any battery chemistry and represent a particularly critical competitive advantage for K-ion batteries.[4] Therefore, we emphasize the necessity of correlating the transport properties and properties of electrode−electrolyte interphases and interfaces in the design of novel K-ion electrolytes.

Additionally, it is of interest to compare the transport properties of KFSI-TEP to those of KFSI in 1,2-dimethoxyethane (DME). KFSI-DME is another promising K-ion electrolyte and the only other nonaqueous K-ion electrolyte that has been fully characterized to date.[56] At a temperature of 20 °C, 2 *m* KFSI-DME exhibits a higher diffusion coefficient and ionic conductivity ($D \approx 5.5 \times 10^{-10}$ m^2 s^{-1}, $\kappa \approx 16$ mS cm^{-1}), surpassing those of 2 *m* KFSI-TEP by an order of magnitude. These differences are likely caused by the significantly higher viscosity of TEP compared to DME. The thermodynamic factor of 2 *m* KFSI-DME (~1.9) is lower than that of 2 *m* KFSI-TEP, as might be expected from the higher dielectric constant, ε_r, of TEP (ε_r = 13.0 and 7.2 for TEP and DME, respectively[61]), resulting in TEP having greater solvating power[62] and shielding the ion−ion interactions that reduce χ_M at low concentration. The cation transference number ($t_+^0 \approx$ 0.35 for 2 *m* KFSI-DME) shows no significant difference between the two electrolyte systems. Overall, this highlights that the choice of solvent can have a large impact on electrolyte transport and thermodynamic properties, which will have a significant impact on subsequent cell performance, as recently demonstrated by Dhir et al. through full-cell KIB modeling.[60] The implementation of accurate electrolyte characterization techniques like ORGA will therefore be invaluable during the development of future electrolytes to aid in the commercialization of K-ion batteries.

5. CONCLUSION

In summary, this study optimized and validated operando Raman gradient analysis (ORGA) as a promising comprehensive characterization technique. Through optimized laser settings, potassium metal pretreatment, theoretical model refinement, and fitting strategy enhancement, the research ultimately presents a successful case of concentration gradient visualization and improved fitting for the K|KFSI-TEP|K electrochemical system. Furthermore, the simultaneous use of traditional methods and the ORGA method characterizes the transport and thermodynamic properties of one of the most promising potassium-ion battery electrolytes, KFSI-TEP, for the first time. The results affirm the excellent reproducibility of the visualization method and its consistency with those of leading conventional methods. The comparative analysis highlights the operational simplicity, reduced consumption, and shorter overall experimental time of ORGA. Practically, it stands out as a fast and efficient comprehensive electrolyte characterization technique. Lastly, the measured concentration dependence of the properties provides deeper insights into the transport behavior of this leading K-ion electrolyte and furnishes critical properties for battery modeling, thereby assisting in the design of future promising high-performance potassium-ion batteries.

■ ASSOCIATED CONTENT

Supporting Information

The Supporting Information is available free of charge at https://pubs.acs.org/doi/10.1021/acsenergylett.4c00661.

Experimental procedures, including materials, operando Raman gradient analysis (ORGA), and conventional methods, supplementary data, including ORGA setup and analysis, laser power optimization, densitometry, conventional methods, and viscosity measurements, and supplementary notes, including error analysis, theory, and model derivation (PDF)

■ AUTHOR INFORMATION

Corresponding Author

Mauro Pasta − *Department of Materials, University of Oxford, Oxford OX1 3PH, U.K.;* orcid.org/0000-0002-2613-4555; Email: mauro.pasta@materials.ox.ac.uk

https://doi.org/10.1021/acsenergylett.4c00661
ACS Energy Lett. 2024, 9, 1537−1544

Authors

Junyi Zhao − *Department of Materials, University of Oxford, Oxford OX1 3PH, U.K.*

Ben Jagger − *Department of Materials, University of Oxford, Oxford OX1 3PH, U.K.*

Lorenz F. Olbrich − *Department of Materials, University of Oxford, Oxford OX1 3PH, U.K.*

Johannes Ihli − *Department of Materials, University of Oxford, Oxford OX1 3PH, U.K.*

Shobhan Dhir − *Department of Materials, University of Oxford, Oxford OX1 3PH, U.K.*

Maxim Zyskin − *Department of Materials, University of Oxford, Oxford OX1 3PH, U.K.*

Xinyao Ma − *Department of Materials, University of Oxford, Oxford OX1 3PH, U.K.*

Complete contact information is available at: https://pubs.acs.org/10.1021/acsenergylett.4c00661

Author Contributions

[†]B.J. and L.F.O. contributed equally.

Notes

The authors declare the following competing financial interest(s): M.P. is a scientific advisor of Project K Energy, Inc.

■ ACKNOWLEDGMENTS

The authors would like to acknowledge the financial support of the Henry Royce Institute (through UK Engineering and Physical Sciences Research Council grant EP/R010145/1) for capital equipment. B.J. is grateful for the support of the Clarendon Fund Scholarships. L.F.O. was supported by funding from the Engineering and Physical Sciences Research Council (grant EP/R511742/1). S.D. appreciates the financial support from EPSRC and Shell. X.M. is grateful for the support of China Scholarship Council-University of Oxford Scholarship.

■ REFERENCES

(1) IEA. *Global EV Outlook 2022*; 2022. https://www.iea.org/reports/global-ev-outlook-2022 (accessed 2024-03-08).

(2) IEA. *The Role of Critical Minerals in Clean Energy Transitions*; 2021. https://www.iea.org/reports/the-role-of-critical-minerals-in-clean-energy-transitions (accessed 2024-03-08).

(3) Frith, J. T.; Lacey, M. J.; Ulissi, U. A non-academic perspective on the future of lithium-based batteries. *Nat. Commun.* **2023**, *14*, 420.

(4) Dhir, S.; Wheeler, S.; Capone, I.; Pasta, M. Outlook on K-Ion Batteries. *Chem.* **2020**, *6*, 2442−2460.

(5) Hosaka, T.; Kubota, K.; Hameed, A. S.; Komaba, S. Research Development on K-Ion Batteries. *Chem. Rev.* **2020**, *120*, 6358−6466.

(6) Sada, K.; Darga, J.; Manthiram, A. Challenges and Prospects of Sodium-Ion and Potassium-Ion Batteries for Mass Production. *Adv. Energy Mater.* **2023**, *13*, 2302321.

(7) Tan, H.; Lin, X. Electrolyte Design Strategies for Non-Aqueous High-Voltage Potassium-Based Batteries. *Molecules* **2023**, *28*, 823.

(8) Logan, E. R.; Tonita, E. M.; Gering, K. L.; Li, J.; Ma, X.; Beaulieu, L. Y.; Dahn, J. R. A Study of the Physical Properties of Li-Ion Battery Electrolytes Containing Esters. *J. Electrochem. Soc.* **2018**, *165*, A21.

(9) Valøen, L. O.; Reimers, J. N. Transport Properties of $LiPF_6$-Based Li-Ion Battery Electrolytes. *J. Electrochem. Soc.* **2005**, *152*, A882.

(10) Landesfeind, J.; Gasteiger, H. A. Temperature and Concentration Dependence of the Ionic Transport Properties of Lithium-Ion Battery Electrolytes. *J. Electrochem. Soc.* **2019**, *166*, A3079.

(11) Uemura, S.; Komiyama, S.; Kotaka, T.; Aoki, O.; Suga, S.; Tabuchi, Y.; Hirai, S. Quantitative Measurement of Ion Transport Phenomena in an Operating Lithium-Ion Battery by Low-Energy X-ray Microscopy and Nuclear Magnetic Resonance Spectroscopy. *J. Power Sources* **2021**, *491*, 229601.

(12) Stewart, S. G.; Newman, J. The Use of UV/vis Absorption to Measure Diffusion Coefficients in $LiPF_6$ Electrolytic Solutions. *J. Electrochem. Soc.* **2008**, *155*, F13.

(13) Brissot, C.; Rosso, M.; Chazalviel, J.-N.; Lascaud, S. Concentration Measurements in Lithium/Polymer−Electrolyte/Lithium Cells During Cycling. *J. Power Sources* **2001**, *94*, 212−218.

(14) Mistry, A.; Srinivasan, V.; Steinrück, H.-G. Characterizing Ion Transport in Electrolytes via Concentration and Velocity Profiles. *Adv. Energy Mater.* **2023**, *13*, 2203690.

(15) Steinrück, H.-G.; et al. Concentration and Velocity Profiles in a Polymeric Lithium-Ion Battery Electrolyte. *Energy Environ. Sci.* **2020**, *13*, 4312−4321.

(16) Klett, M.; Giesecke, M.; Nyman, A.; Hallberg, F.; Lindström, R. W.; Lindbergh, G.; Furó, I. Quantifying Mass Transport during Polarization in a Li Ion Battery Electrolyte by In Situ ^{7}Li NMR Imaging. *J. Am. Chem. Soc.* **2012**, *134*, 14654−14657.

(17) Newman, J.; Thomas-Alyea, K. *Electrochemical Systems*, 3rd ed.; Wiley: 2004; The ECS Series of Texts and Monographs.

(18) Robinson, R. A.; Stokes, R. H. *Electrolyte Solutions*, 2nd ed.; Dover Publications: 2002.

(19) Newman, J.; Chapman, T. W. Restricted Diffusion in Binary Solutions. *AIChE J.* **1973**, *19*, 343−348.

(20) Hou, T.; Monroe, C. W. Composition-Dependent Thermodynamic and Mass-Transport Characterization of Lithium Hexafluorophosphate in Propylene Carbonate. *Electrochim. Acta* **2020**, *332*, 135085.

(21) Hafezi, H.; Newman, J. Verification and Analysis of Transference Number Measurements by the Galvanostatic Polarization Method. *J. Electrochem. Soc.* **2000**, *147*, 3036.

(22) Stejskal, E. O. Use of Spin Echoes in a Pulsed Magnetic-Field Gradient to Study Anisotropic, Restricted Diffusion and Flow. *J. Chem. Phys.* **1965**, *43*, 3597−3603.

(23) Fouache-Ayoub, S.; Garreau, M.; Prabhu, P. V. S. S.; Thevenin, J. Mass-Transport Properties of Lithium Surface Layers Formed in Sulfolane-Based Electrolytes. *J. Electrochem. Soc.* **1990**, *137*, 1659.

(24) Wang, A. A.; O'Kane, S. E. J.; Planella, F. B.; Houx, J. L.; O'Regan, K.; Zyskin, M.; Edge, J.; Monroe, C. W.; Cooper, S. J.; Howey, D. A.; Kendrick, E.; Foster, J. M. Review of Parameterisation and a Novel Database (LiionDB) for Continuum Li-Ion Battery Models. *Prog. Energy* **2022**, *4*, 032004.

(25) Ma, Y.; Doyle, M.; Fuller, T. F.; Doeff, M. M.; Jonghe, L. C. D.; Newman, J. The Measurement of a Complete Set of Transport Properties for a Concentrated Solid Polymer Electrolyte Solution. *J. Electrochem. Soc.* **1995**, *142*, 1859.

(26) Bruce, P. G.; Vincent, C. A. Steady State Current Flow in Solid Binary Electrolyte Cells. *J. Electroanal. Chem. Interface Electrochem.* **1987**, *225*, 1−17.

(27) Balsara, N. P.; Newman, J. Relationship Between Steady-State Current in Symmetric Cells and Transference Number of Electrolytes Comprising Univalent and Multivalent Ions. *J. Electrochem. Soc.* **2015**, *162*, A2720.

(28) Pesko, D. M.; Timachova, K.; Bhattacharya, R.; Smith, M. C.; Villaluenga, I.; Newman, J.; Balsara, N. P. Negative Transference Numbers in Poly(ethylene oxide)-Based Electrolytes. *J. Electrochem. Soc.* **2017**, *164*, No. E3569.

(29) Rosenwinkel, M. P.; Schönhoff, M. Lithium Transference Numbers in PEO/LiTFSA Electrolytes Determined by Electrophoretic NMR. *J. Electrochem. Soc.* **2019**, *166*, A1977.

(30) MacInnes, D. A.; Cowperthwaite, I. A.; Huang, T. C. The Moving-Boundary Method for Determining Transference Numbers: VI. Further Developments in Experimental Technique. *J. Am. Chem. Soc.* **1927**, *49*, 1710−1717.

(31) Ding, M. S.; Xu, K.; Zhang, S. S.; Amine, K.; Henriksen, G. L.; Jow, T. R. Change of Conductivity with Salt Content, Solvent Composition, and Temperature for Electrolytes of $LiPF_6$ in Ethylene Carbonate-Ethyl Methyl Carbonate. *J. Electrochem. Soc.* **2001**, *148*, A1196.

(32) Wang, A. A.; Hou, T.; Karanjavala, M.; Monroe, C. W. Shifting-Reference Concentration Cells to Refine Composition-Dependent Transport Characterization of Binary Lithium-Ion Electrolytes. *Electrochim. Acta* **2020**, *358*, 136688.
(33) Stewart, S.; Newman, J. Measuring the Salt Activity Coefficient in Lithium-Battery Electrolytes. *J. Electrochem. Soc.* **2008**, *155*, A458.
(34) Kim, S. U.; Srinivasan, V. A Method for Estimating Transport Properties of Concentrated Electrolytes from Self-Diffusion Data. *J. Electrochem. Soc.* **2016**, *163*, A2977.
(35) Mistry, A.; Srinivasan, V. Do We Need an Accurate Understanding of Transport in Electrolytes? *Joule* **2021**, *5*, 2773–2776.
(36) Chang, H. J.; Ilott, A. J.; Trease, N. M.; Mohammadi, M.; Jerschow, A.; Grey, C. P. Correlating Microstructural Lithium Metal Growth with Electrolyte Salt Depletion in Lithium Batteries Using ^{7}Li MRI. *J. Am. Chem. Soc.* **2015**, *137*, 15209–15216.
(37) Klamor, S.; Zick, K.; Oerther, T.; Schappacher, F. M.; Winter, M.; Brunklaus, G. ^{7}Li In Situ 1D NMR Imaging of a Lithium Ion Battery. *Phys. Chem. Chem. Phys.* **2015**, *17*, 4458–4465.
(38) Bazak, J. D.; Allen, J. P.; Krachkovskiy, S. A.; Goward, G. R. Mapping of Lithium-Ion Battery Electrolyte Transport Properties and Limiting Currents with In Situ MRI. *J. Electrochem. Soc.* **2020**, *167*, 140518.
(39) Sethurajan, A. K.; Krachkovskiy, S. A.; Halalay, I. C.; Goward, G. R.; Protas, B. Accurate Characterization of Ion Transport Properties in Binary Symmetric Electrolytes Using In Situ NMR Imaging and Inverse Modeling. *J. Phys. Chem. B* **2015**, *119*, 12238–12248.
(40) Chandrashekar, S.; Oparaji, O.; Yang, G.; Hallinan, D. Communication—^{7}Li MRI Unveils Concentration Dependent Diffusion in Polymer Electrolyte Batteries. *J. Electrochem. Soc.* **2016**, *163*, A2988.
(41) Krachkovskiy, S. A.; Bazak, J. D.; Werhun, P.; Balcom, B. J.; Halalay, I. C.; Goward, G. R. Visualization of Steady-State Ionic Concentration Profiles Formed in Electrolytes during Li-Ion Battery Operation and Determination of Mass-Transport Properties by In Situ Magnetic Resonance Imaging. *J. Am. Chem. Soc.* **2016**, *138*, 7992–7999.
(42) Wang, A. A.; Gunnarsdóttir, A. B.; Fawdon, J.; Pasta, M.; Grey, C. P.; Monroe, C. W. Potentiometric MRI of a Superconcentrated Lithium Electrolyte: Testing the Irreversible Thermodynamics Approach. *ACS Energy Lett.* **2021**, *6*, 3086–3095.
(43) Grundy, L. S.; Galluzzo, M. D.; Loo, W. S.; Fong, A. Y.; Balsara, N. P.; Takacs, C. J. Inaccessible Polarization-Induced Phase Transitions in a Block Copolymer Electrolyte: An Unconventional Mechanism for the Limiting Current. *Macromolecules* **2022**, *55*, 7637–7649.
(44) Galluzzo, M. D.; Grundy, L. S.; Takacs, C. J.; Cao, C.; Steinrück, H.-G.; Fu, S.; Rivas Valadez, M. A.; Toney, M. F.; Balsara, N. P. Orientation-Dependent Distortion of Lamellae in a Block Copolymer Electrolyte under DC Polarization. *Macromolecules* **2021**, *54*, 7808–7821.
(45) Takamatsu, D.; Yoneyama, A.; Asari, Y.; Hirano, T. Quantitative Visualization of Salt Concentration Distributions in Lithium-Ion Battery Electrolytes during Battery Operation Using X-ray Phase Imaging. *J. Am. Chem. Soc.* **2018**, *140*, 1608–1611.
(46) Dawkins, J. I. G.; Ghavidel, M. Z.; Chhin, D.; Beaulieu, I.; Hossain, M. S.; Feng, R.; Mauzeroll, J.; Schougaard, S. B. Operando Tracking of Solution-Phase Concentration Profiles in Li-Ion Battery Positive Electrodes Using X-ray Fluorescence. *Anal. Chem.* **2020**, *92*, 10908–10912.
(47) Rey, I.; Bruneel, J.; Grondin, J.; Servant, L.; Lassègues, J. Raman Spectroelectrochemistry of a Lithium/Polymer Electrolyte Symmetric Cell. *J. Electrochem. Soc.* **1998**, *145*, 3034.
(48) Fawdon, J.; Ihli, J.; La Mantia, F.; Pasta, M. Characterising Lithium-Ion Electrolytes via Operando Raman Microspectroscopy. *Nat. Commun.* **2021**, *12*, 4053.
(49) Fawdon, J.; Rees, G. J.; La Mantia, F.; Pasta, M. Insights into the Transport and Thermodynamic Properties of a Bis-(fluorosulfonyl)imide-Based Ionic Liquid Electrolyte for Battery Applications. *J. Phys. Chem. Lett.* **2022**, *13*, 1734–1741.
(50) Georén, P.; Adebahr, J.; Jacobsson, P.; Lindbergh, G. Concentration Polarization of a Polymer Electrolyte. *J. Electrochem. Soc.* **2002**, *149*, A1015.
(51) Nisancioglu, K.; Newman, J. Diffusion in Aqueous Nitric Acid Solutions. *AIChE J.* **1973**, *19*, 797–801.
(52) Jafta, C. J.; Sun, X.-G.; Veith, G. M.; Jensen, G. V.; Mahurin, S. M.; Paranthaman, M. P.; Dai, S.; Bridges, C. A. Probing Microstructure and Electrolyte Concentration Dependent Cell Chemistry via Operando Small Angle Neutron Scattering. *Energy Environ. Sci.* **2019**, *12*, 1866–1877.
(53) Deng, L.; Wang, T.; Hong, Y.; Feng, M.; Wang, R.; Zhang, J.; Zhang, Q.; Wang, J.; Zeng, L.; Zhu, Y.; Guo, L. A Nonflammable Electrolyte Enabled High Performance $K_{0.5}MnO_2$ Cathode for Low-Cost Potassium-Ion Batteries. *ACS Energy Lett.* **2020**, *5*, 1916–1922.
(54) Liu, S.; Mao, J.; Zhang, Q.; Wang, Z.; Pang, W. K.; Zhang, L.; Du, A.; Sencadas, V.; Zhang, W.; Guo, Z. An Intrinsically Non-flammable Electrolyte for High-Performance Potassium Batteries. *Angew. Chem., Int. Ed.* **2020**, *59*, 3638–3644.
(55) Liang, H.-J.; Gu, Z.-Y.; Zhao, X.-X.; Guo, J.-Z.; Yang, J.-L.; Li, W.-H.; Li, B.; Liu, Z.-M.; Sun, Z.-H.; Zhang, J.-P.; Wu, X.-L. Advanced Flame-Retardant Electrolyte for Highly Stabilized K-Ion Storage in Graphite Anode. *Sci. Bull.* **2022**, *67*, 1581–1588.
(56) Dhir, S.; Jagger, B.; Maguire, A.; Pasta, M. Fundamental Investigations on the Ionic Transport and Thermodynamic Properties of Non-Aqueous Potassium-Ion Electrolytes. *Nat. Commun.* **2023**, *14*, 3833.
(57) Ma, M.; Chen, B.; Pan, H. Three-Dimensional Heterogeneity in Liquid Electrolyte Structures Promotes Na Ion Transport and Storage Performance in Na-Ion Batteries. *Chem. Sci.* **2023**, *14*, 5983–5991.
(58) Zeng, Z.; Murugesan, V.; Han, K. S.; Jiang, X.; Cao, Y.; Xiao, L.; Ai, X.; Yang, H.; Zhang, J.-G.; Sushko, M. L.; Liu, J. Non-Flammable Electrolytes with High Salt-to-Solvent Ratios for Li-Ion and Li-Metal Batteries. *Nat. Energy* **2018**, *3*, 674–681.
(59) Yu, Z.; Balsara, N. P.; Borodin, O.; Gewirth, A. A.; Hahn, N. T.; Maginn, E. J.; Persson, K. A.; Srinivasan, V.; Toney, M. F.; Xu, K.; Zavadil, K. R.; Curtiss, L. A.; Cheng, L. Beyond Local Solvation Structure: Nanometric Aggregates in Battery Electrolytes and Their Effect on Electrolyte Properties. *ACS Energy Letters* **2022**, *7*, 461–470.
(60) Dhir, S.; Cattermull, J.; Jagger, B.; Schart, M.; Olbrich, L.; Chen, Y.; Zhao, J.; Sada, K.; Goodwin, A.; Pasta, M. Characterisation and Modelling of Potassium-Ion Batteries. *Research Square*, 2024-01-08. https://www.researchsquare.com/article/rs-3734005/v1 (accessed 2024-03-08).
(61) Zeng, G.; Xiong, S.; Qian, Y.; Ci, L.; Feng, J. Non-Flammable Phosphate Electrolyte with High Salt-to-Solvent Ratios for Safe Potassium-Ion Battery. *J. Electrochem. Soc.* **2019**, *166*, A1217.
(62) Zhang, F.; Wang, X.; Wu, M.; Yang, A.; Li, Y.; Man, M.; Li, Y.; Guo, J. Weakly Solvated Electrolyte Driven Anion Interface Chemistry for Potassium Batteries/Hybrid Capacitors. *ACS Energy Lett.* **2023**, *8*, 4895–4902.

https://doi.org/10.1021/acsenergylett.4c00661
ACS Energy Lett. 2024, 9, 1537–1544